JOURNAL OF GEOPHYSICAL RESEARCH, VOL. 113, C05020, doi:10.1029/2007JC004182, 2008

Click Here for Full Article

Effect of heat transmission through melt ponds and ice on melting during summer in the Arctic Ocean

Jun Inoue,[1] Takashi Kikuchi,[1] and Donald K. Perovich[2]

Received 22 February 2007; revised 11 November 2007; accepted 16 January 2008; published 16 May 2008.

[1] To observe sea ice and ocean conditions in the Arctic in summer, a trans-Arctic research cruise of the U.S. Coast Guard Cutter *Healy* was conducted from 5 August to 30 September 2005. The relationship between the ice concentration observed by the on-board ice-watch and the temperature above the freezing point (ΔT) measured by expendable conductivity-temperature-depth (XCTD) sensors had a negative correlation (CT-relationship) before the onset of freezing. This means that as ice concentration decreases, ΔT increases due to the larger absorption of solar radiation. However, ΔT in high ice-covered regions (>90%) remains more than 0.1 K during the melting season, suggesting that sea-ice and melt-pond areas work as heat source areas as well as leads. By separating the effects of heat input from open water, melt ponds, and ice on the heating of mixed layers, we found that the contribution of the transmitted heat through ponds and ice on the ΔT-gain is large in highly ice-covered regions. To examine the effect of such heating on ice melting, a simplified ice-ocean-coupled model was applied. By changing the heat input to obtain the analyzed ΔT-gain for each surface category, the transmittances of ponds and ice were indirectly estimated as 55% and 9%, respectively. After including the effects of transmitted heat through ponds and ice, the modeled results agreed with the observed CT-relationship. Comparisons between the results of turning on and off the effect of transmitted heat through ponds and ice showed that it amplified the open water-albedo feedback mechanism in the highly ice-covered region.

Citation: Inoue, J., T. Kikuchi, and D. K. Perovich (2008), Effect of heat transmission through melt ponds and ice on melting during summer in the Arctic Ocean, *J. Geophys. Res.*, *113*, C05020, doi:10.1029/2007JC004182.

1. Introduction

[2] The interaction between sea ice and heat input from the atmosphere is one of the most important processes contributing to declining ice cover during summertime in the Arctic [e.g., *Curry et al.*, 1995]. Because shortwave (SW) radiation is a main source of heat input in the Arctic, it is important to determine how SW radiation is distributed within the atmosphere-ice-ocean system and how this distribution affects heat and mass exchanges within the system. Because of the importance of albedo to the surface heat budget of sea ice, a considerable number of studies for a wide range of ice types and conditions have demonstrated that the variability of the albedos is linked to a strong dependence on surface conditions and the structure of the ice [e.g., *Grenfell and Maykut*, 1977; *Grenfell and Perovich*, 1984, 2004; *Hanesiak et al.*, 2001].

[3] The SW radiation that penetrates into open water can become the dominant heat source for ocean surface warming and consequent lateral and bottom melting of sea ice [*Maykut and Perovich*, 1987; *Maykut and McPhee*, 1995]. Using a drifting buoy, *McPhee et al.* [2003] showed that heat flux below the Arctic sea ice is dominated by the storage and release of SW radiation energy in the ocean boundary layer during summer. The effect of wind speed on lateral and bottom melting has also been investigated [e.g., *Richter-Menge et al.*, 2001; *Inoue and Kikuchi*, 2006]. While much of the solar energy is transmitted to the ocean through leads, substantial portions are also transmitted through bare ice and ponded ice. *Perovich* [2005] showed that the energy transmitted to the ocean reached a maximum near the end of the melt season in mid-August when the albedo and ice thickness were at their minima and lead and pond fractions were at their maxima. He also showed that observed pond transmittance jumped from near 0 to 0.2 after the onset of melting and monotonically increased up to 0.4–0.5 during the summer as the ice beneath the pond thinned. In his observations, a sharp decrease in pond transmittance was also observed after the onset of freezing and snowfall. Bare ice transmittances, on the other hand, were smaller than pond transmittances (~0.2).

[4] Although satellite passive microwave sensors are very useful for revealing Arctic sea ice changes, their resolutions are too coarse to distinguish open water from ponded ice. Hence total ice concentrations determined by these devices are not as accurate during the summer melt season as in winter [*Cavalieri et al.*, 1984; *Fetterer and Untersteiner*,

[1]Institute of Observational Research for Global Change, Japan Agency for Marine-Earth Science and Technology, Yokosuka, Japan.
[2]Engineer Research and Development Center, Cold Regions Research and Engineering Laboratory, Hanover, New Hampshire, USA.

Copyright 2008 by the American Geophysical Union.
0148-0227/08/2007JC004182$09.00

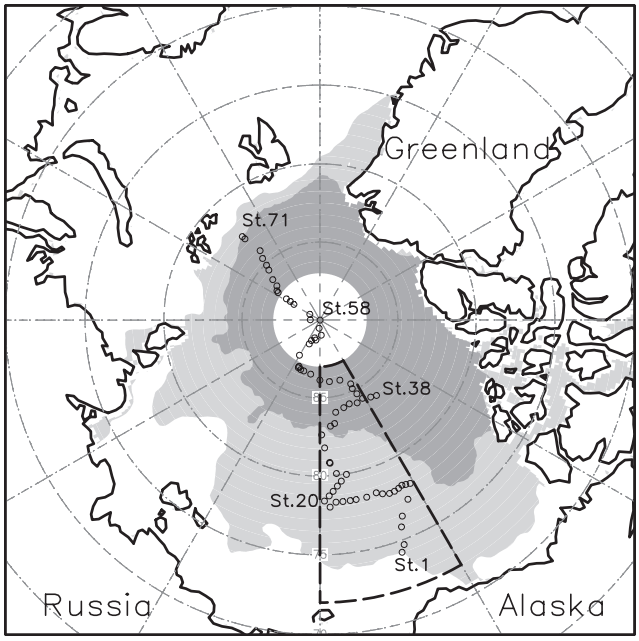

Figure 1. Cruise track of USCGC *Healy* and the XCTD stations. Light and dark shadings denote mean ice concentrations during August 2005 greater than 30% and 90%, respectively. The area enclosed by the dashed line is shown again in Figure 3.

1998]. While satellite visible-band sensors have higher resolution, the persistent cloud cover over the ice pack during the summer [e.g., *Intrieri et al.*, 2002; *Inoue et al.*, 2005a] severely limits the utility of these sensors to observe melt ponds. To understand the relationship between recent ice decay and the ice-upper ocean coupled system, observations of ice and ocean conditions in various areas of the Arctic must be obtained.

[5] In the Antarctic, ice concentration is negatively correlated with temperature and positively correlated with salinity for spatially averaged data, suggesting that the local balances of heat and salt nearly hold in a bulk area [*Ohshima et al.*, 1998]. This relationship has been investigated and explained by a simplified coupled model of the ice and upper ocean [*Ohshima and Nihashi*, 2005; *Nihashi et al.*, 2005]. In contrast, very few observational studies have examined the ice-upper ocean-coupled system in the Arctic, although a simple ice-upper ocean-coupled model has been developed [e.g., *Steele*, 1992]. Using one-dimensional sea ice model, *Ebert et al.* [1995] found that melt ponds increase the penetration of SW radiation into the ice interior by 50%, depending on the fractional coverage and depth of ponds, and increase the transmission of incoming SW radiation into the upper ocean relative to unponded ice. As for climate modeling, sea-ice processes are influenced by differences in the albedo parameterizations [*Liu et al.*, 2006]. Therefore an explicit treatment of melt ponds in the models is needed for a correct simulation of the sea-ice albedo feedback [*Curry et al.*, 1995, 2001]. However, there has not been an adequate ocean data set to evaluate the effects of surface conditions on sea-ice melting.

[6] To understand the interaction of ice with ponds in the upper ocean system, observations from an ice-breaker are essential to simultaneously monitor the characteristics of the ice surface and upper ocean. From the beginning of August 2005 until the end of September 2005, we observed sea-ice cover and upper ocean conditions across the Arctic Ocean from the USCGC *Healy* (Figure 1). Here we describe sea-ice melting processes based on various sea-ice and upper ocean data collected in the summertime Arctic and compare the data to the results of a simple ice-upper ocean-coupled model.

2. Observations

[7] The USCGC *Healy* trans-Arctic cruise in 2005 presented a unique opportunity to obtain sectional data across the Arctic Ocean [*Darby et al.*, 2005]. The *Healy* departed Dutch Harbor, Alaska, on 5 August and tracked across the western and northwestern perimeter of the Canadian Basin. The ship passed across the North Pole on 11–12 September and arrived at Tromso, Norway, on 30 September. This track enabled us to observe oceanic and sea-ice conditions across the Arctic Ocean, and to record basic meteorological conditions (e.g., air temperature, humidity, and wind).

[8] Expendable conductivity-temperature-depth (XCTD) sensors and processing equipment (Tsurumi-Seiki Co., Ltd., Yokohama, Japan) measured temperature and conductivity (i.e., salinity) from the sea surface to a depth of 1100 m. An XCTD probe launched from the ship into the water sank at a constant rate while measuring temperature and conductivity. We launched XCTD sensors at 71 observational sites across the Arctic Ocean (see Figure 1). The first 38 observations were conducted on the western and northwestern perimeter of the Canadian Basin. These sites were located over or across the major ridges around the Canadian Basin. The final 33 stations were located across the central and eastern Arctic Ocean.

[9] Bi-hourly visual observations of sea-ice cover were made according to the method of *Worby and Allison* [1999] from the bridge while the ship was moving through the pack ice (Figure 2). For each visual observation, the sea-ice cover was divided into three thickness categories for which we estimated the ice concentration, ice type, and mean snow depth on unridged ice. In this study, we used data for the fractions of open water (A_o), ponds (A_p), ice (A_i), and ice thickness, as well as daily ice concentration data derived from the Special Sensor Microwave Imager (SSM/I) on the Defense Meteorological Satellite Program (DMSP) F13 at a grid resolution of 25 km.

3. Ice and Ocean Conditions

[10] Figure 3 shows the time-latitude cross-section of the ice concentration averaged between 150°W and 180°W, corresponding to the cruise to the North Pole. Near the Alaskan coast (72°N), the ice concentration started to decrease in the middle of July, and the highly ice-covered area (i.e., 90%) retreated rapidly northward until mid-August. The cruise of USCGC *Healy* started when sea-ice melting was predominant. We moved northward up to Northwind Ridge (78.5°N) under moderate ice concentrations (70%). After traveling westward along the same latitude (Figure 1), the ship turned northward again and finally entered the highly ice-covered area (over 90%) after 23 August. During this period, the incoming SW radiation,

Figure 2. Panoramic photograph of the ice cover taken from the flying bridge of the *Healy* on 14 August 2005 at 78.193°N, 153.548°W.

which can be approximated as one-third the value of SW radiation at the top of the atmosphere [*Inoue et al.*, 2005b], decreased from 130 to 90 W m^{-2}. However, the latitudinal gradient was very weak, suggesting that the heat input into the upper ocean was almost the same during the summer.

[11] Figure 4 shows some of the vertical XCTD profiles. The water structure was not uniform across the Arctic Ocean. The Canadian Basin (e.g., St. 5 at 77.2°N, 153.9°W) had a complex temperature profile as noted by *Shimada et al.* [2001]. In almost all areas, however, temperature and salinity were approximately uniform from near the surface to a depth of at least 10 m. That is, the summer surface mixed layer in the Arctic Ocean had a thickness of more than 10 m. From these vertical profiles, we could assume that the temperature and salinity between 5 and 10 m approximately represented the values averaged over the surface mixed layer as a whole because the layer is commonly affected by sea-ice melting for all profiles.

[12] Figure 5 shows the time series of the observed atmosphere, ice, and ocean characteristics along the cruise tracks. The sea-ice condition was complicated because of the melt ponds. The ponded area covered approximately 25% of the sea-ice area during August (Figure 5c) but then decreased due to freezing as the air temperature dropped below zero (Figure 5b). Although two major algorithms provided the basic temporal/spatial evolution of ice concentration near the ship, the high ponded fraction made satellite-derived ice cover estimations unreliable. The ice concentration derived from the Bootstrap Algorithm [*Comiso*, 1990] appears to include the ponded area (open squares), which is the same feature reported by *Inoue et al.* [2008], while that from the NASA Team Algorithm [*Cavalieri et al.*, 1990] seems to be partly affected by

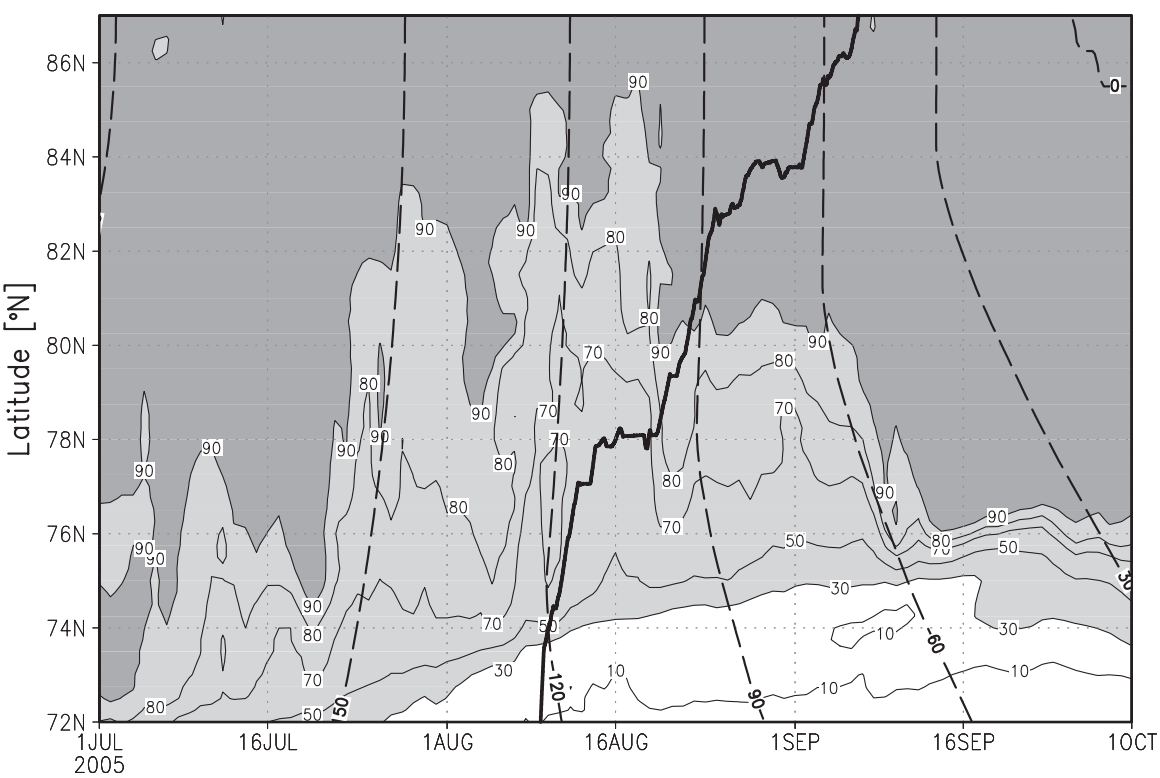

Figure 3. Time-latitude cross-section of the ice concentration (%) averaged between 150°W and 180°W, derived from the DMSP SSM/I. The thick solid and dashed lines denote the cruise track of the *Healy* and one-third the value of the daily mean shortwave radiation (W m^{-2}) at the top of the atmosphere, respectively.

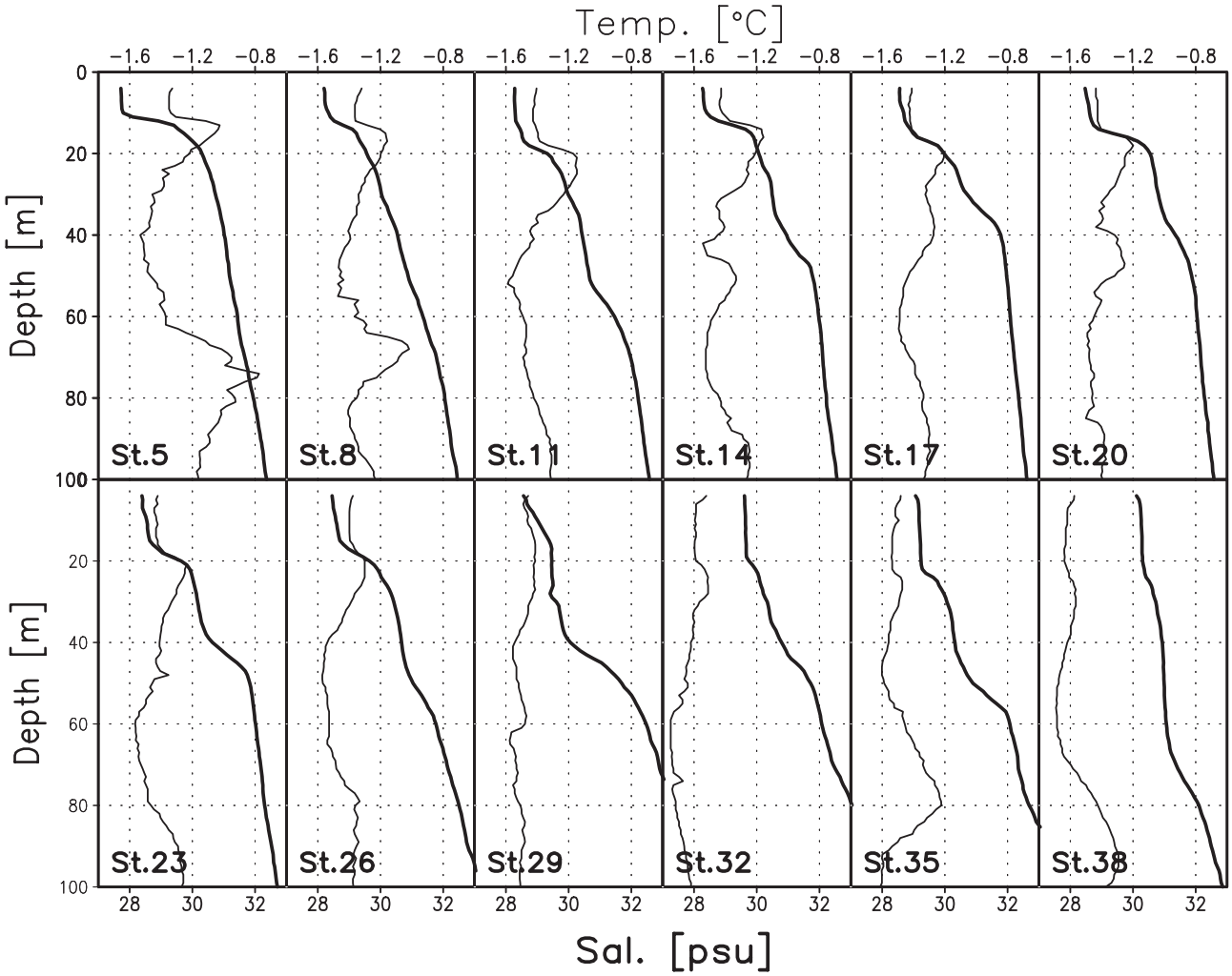

Figure 4. Vertical profiles of the water temperature (thin line) and salinity (thick line) obtained by the XCTD sensors. Corresponding axes of temperature and salinity are indicated at the top and bottom, respectively, of each panel. Locations of the stations are indicated in Figure 1.

melt ponds (closed circles). In general, ice thickness increased from 1 to 2 m as the ship moved northward (Figure 5d). The proportion of FYI and MYI observed by ice watch during August was 59% and 41%, respectively. MYI dominated after 18 August (>78°N).

[13] To determine how much the upper ocean was heated by the atmosphere (i.e., incoming solar radiation), the temperature above the freezing point (ΔT) is a useful parameter, particularly in areas where salinity is not horizontally uniform (see Figure 4). ΔT, averaged from 5 to 10 m, was relatively high in the southern region below 80°N (Figure 5e) where the ice concentration was relatively low (e.g., 50–60%). This suggests that incoming solar radiation was absorbed in the open water and some of this radiation was used in the bottom and lateral melting of sea-ice, while the remainder increased the temperature.

4. Relationship Between Ice Concentration and Water Temperature

4.1. CT-Plot

[14] We examined the relationship between the ice concentration (ponds and ice fractions: $A_p + A_i$) observed by the on-board ice-watch and the upper ocean XCTD data, which is useful for understanding the heat balance of atmospheric heat inputs, sea-ice melting, and heat storage in the ocean mixed layer (hereafter termed the local heat balance). Figure 6 shows the ice concentration plotted against ΔT (hereafter called the CT-relationship) for the XCTD casts before the onset of freezing, i.e., during August (Sts. 1 and 38). The visually observed ice concentrations were averaged to daily values to reduce any observer bias. ΔT increased as the ice concentration decreased, which is consistent with results obtained from an Antarctic cruise off Syowa Station [*Ohshima et al.*, 1998] and in the Ross Sea [*Nihashi et al.*, 2005]. Their results have shown that the relationship between ice concentration and the mixed-layer temperature converges with time and that the local heat balance in the ice-upper ocean system approximately holds over that temporal/spatial scale [*Ohshima and Nihashi*, 2005]. In such a case, a process in which ice concentration decreases as ΔT in the upper ocean increases is continued if there is a large absorption of solar radiation (a kind of ice-albedo feedback).

[15] Interestingly, the CT-relationship in our case shows a positive bias (~0.1 K) where the ice concentration is almost

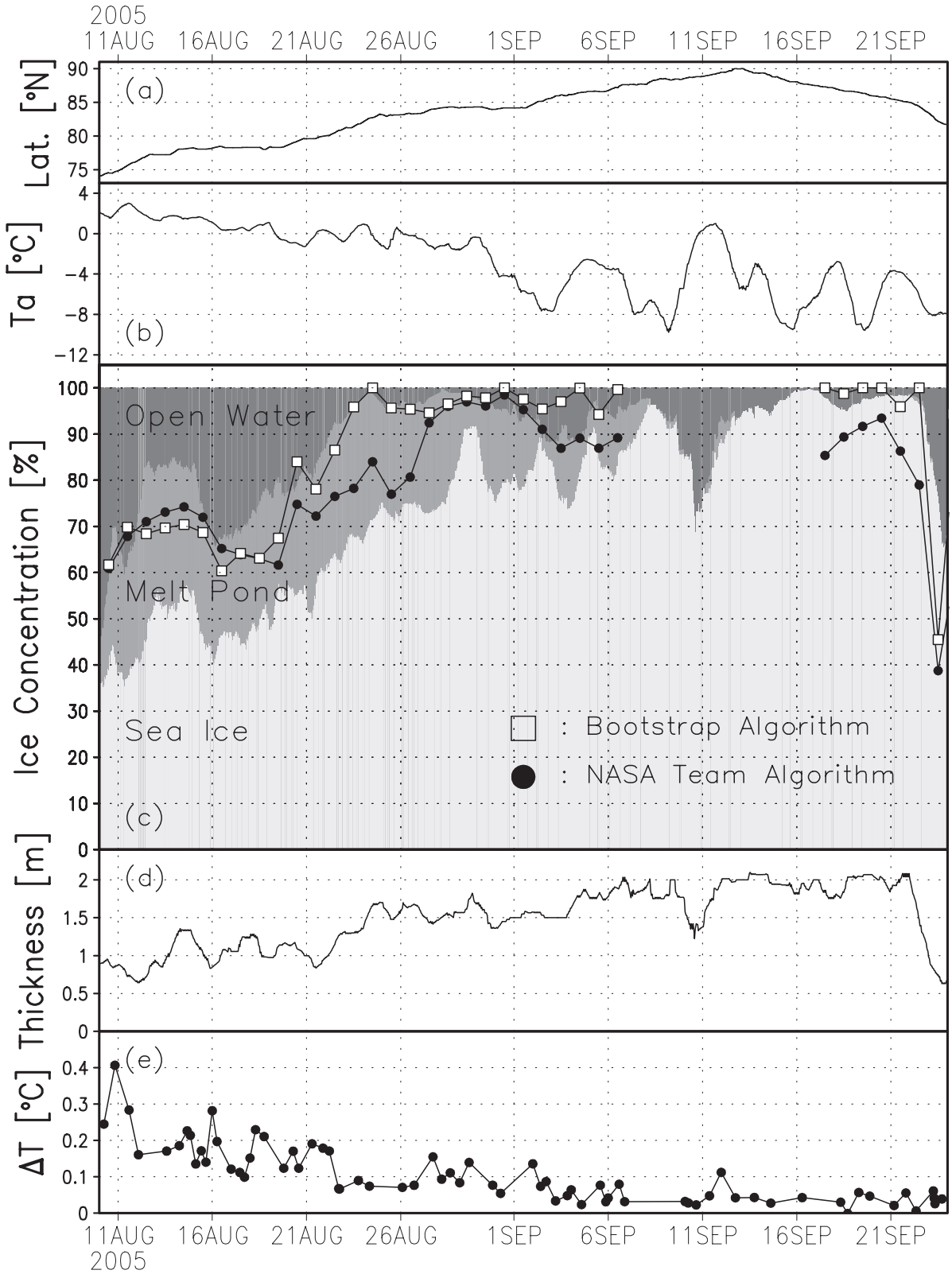

Figure 5. Time series of (a) the latitude cruised by the *Healy*, (b) air temperature obtained on the ship, (c) ice concentration derived from SSM/I data at the closest grid to the ship (open square, Bootstrap Algorithm; closed circle, NASA Team Algorithm), the ice-watch data (dark gray, open water; light gray, melt pond; white, sea ice), (d) ice thickness obtained by the ice-watch, and (e) temperature above the freezing point between 5 and 10 m derived from the XCTD data. The air temperature and ice-watch data were smoothed using a 1-day running mean.

100% denoted by a regression line in Figure 6 (dashed line). This bias is significantly larger than errors resulting from the accuracy in salinity measurements (±0.03 psu causes ±0.02 K in ΔT). These results suggest that the upper ocean gains heat from other sources in addition to the open water area. Solar radiation transmitted through melt pond and sea-ice areas may also affect the ice-upper ocean system.

[16] Because the ice concentration is defined as the sum of pond and ice fractions ($A_p + A_i$), the increase of ΔT (hereafter termed ΔT-gain) by the open water area [$A_o = 1 - (A_p + A_i)$] can be explicitly separated from the total ΔT-gain which is the sum of contributions of open water (ΔT_o), melt ponds (ΔT_p) and ice (ΔT_i). By subtracting the bias resulting from $\Delta T_p + \Delta T_i$(= 0.09 K when $A_p + A_i$ = 100%) from the dashed line in Figure 6 and weighting by $A_p + A_i$, an adjusted regression line for ΔT_o [= ΔT-gain $-0.09 \times (A_p + A_i)$] is obtained (the solid line in Figure 6). The area enclosed between these two lines indicates the $\Delta T_p + \Delta T_i$ induced by $A_p + A_i$. This contribution increases as $A_p + A_i$ becomes large.

4.2. Partitioning of Heat From Open Water, Ponds, and Ice

[17] The benefit of ice-watch data in this research is that A_p is also independently observed. Therefore we also obtained the contribution of ΔT_i to the ΔT-gain explicitly by removing the effect of $\Delta T_o + \Delta T_p$ in the same manner as in Figure 6. Figure 7 shows the relationship between A_i and the ΔT-gain. There is a negative correlation (dashed line), and a bias from ΔT still exists as 0.06 K at the completely ice-covered area without ponds (A_i = 100%). The ΔT_i induced by A_i is also obtained as the shaded area the same way as in Figure 6.

[18] Here we consider the heat partitioning of the ΔT-gain among A_o, A_p, and A_i using the CT-plots. As a specific case, for example, to gain 0.15 K of ΔT when 80% of the area is covered by ice with ponds ($A_p + A_i$: Figure 6), the ΔT-gain is partitioned into ΔT_o = 0.08 K and $\Delta T_p + \Delta T_i$ = 0.07 K, respectively. The ΔT-gain can be also partitioned as the following combination when A_i equals 53% (Figure 7): $\Delta T_o + \Delta T_p$ = 0.12 K and ΔT_i = 0.03 K. Eventually, the ΔT-gain (0.15 K) consists of ΔT_o = 0.08 K from A_o(=20%), ΔT_p = 0.04 K from A_p(=27%), and ΔT_i = 0.03 K from A_i(=53%). In the same way, the heat partitioning under different combinations of surface fractions among A_o, A_p, and A_i is obtained as in Figure 8. Although the contribution of A_o is the main source of heat over most of the area, the roles of A_p and A_i are also relatively large beneath the highly ice-covered area. For example, half of the ΔT-gain comes from ponded and ice-covered areas when $A_p + A_i$ equals 83%. Basically, ΔT_p seems to be nearly constant (~0.05 K) at any $A_p + A_i$ due to less change in A_p as shown in Figure 5c. Considering that A_p is significantly smaller than A_i, the heat transmission through ponded areas may be larger than in ice-covered areas, and smaller than in open water areas because of the difference in albedos between melt ponds and bare ice [e.g., *Grenfell and Maykut*, 1977; *Grenfell and Perovich*, 2004].

5. Role of Heat Transmission Through Ponds and Ice on the Ice-Upper Ocean System

[19] In this section, we developed a simple model to understand the air-ice-sea-coupled system in the summer-time Arctic by focusing on the role of transmitted heat through ponds and ice on the melting processes.

5.1. Model Description

[20] Because heat input into the ice-upper ocean system mainly occurs in open water when ice concentration is relatively low as we showed in the previous section, we began by examining the observed CT-plot using a simple ice-upper ocean-coupled model in which sea-ice bottom and lateral melting is caused only by heat input through open water. Here, we briefly describe the model that was proposed by *Ohshima and Nihashi* [2005]. The upper ocean is simply represented by a layer of thickness H with a uniform temperature T and salinity S. Heat and water exchanges with the ocean below this layer are assumed to be zero due to the strong stratification during the Arctic summer. We implicitly assumed that the open water is well mixed with the water just beneath the ice. The net heat budget on the ice is assumed to be zero; thus, the surface net heat flux would only be supplied in the open water area, 1-A_i. If sea-ice melting is caused by this heat input, the heat balance of the upper ocean can be given by

$$c_w \rho_w H \frac{dT}{dt} = F_n (1 - A_i)(1 - \alpha_o) + L_f \rho_i \left(A_i \frac{dh}{dt} + h \frac{dA_i}{dt} \right), \quad (1)$$

where F_n is the net heat input at the surface, c_w(=3990 J Kg^{-1} K^{-1}) is the heat capacity of seawater, ρ_w(=1026 kg m^{-3}) and ρ_i(=900 kg m^{-3}) are the densities of seawater and sea ice, respectively; t is time, and L_f is the latent heat of fusion for sea ice. The salinity of sea ice in the Arctic is assumed to be 2 psu based on observations in the Arctic multiyear ice [*Eicken et al.*, 1995]. We use a fixed value of L_f = 0.316 MJ kg^{-1}. The ice thickness h is defined as the average thickness; α_o(=0.06) is the surface albedo of open water.

[21] Sea ice melts at the bottom and lateral faces at a rate proportional to the difference between the water temperature and the freezing point (i.e., ΔT). Bottom melting is parameterized as

$$-\rho_i L_f A_i \frac{dh}{dt} = c_w \rho_w A_i c_h u_* \Delta T, \quad (2)$$

where c_h(= 0.0057) and u_*(= 0.0056 m s^{-1}) are the heat transfer coefficient and interface friction velocity obtained from the drifting buoy program of the North Pole Environmental Observatory (NPEO) [*McPhee et al.*, 2003], respectively. Lateral melting is parameterized in a way similar to that of *Hibler* [1979], as

$$\frac{dA_i}{dt} = \frac{dh^*}{dt} \frac{A_i}{2h^*}. \quad (3)$$

In this equation, h^* is defined as an effective ice thickness averaged over each of the grid cells, including the open water fraction. Thus h^* can be regarded as the total ice volume per unit area. Note that the actual averaged thickness is $h = h^*/A_i$ in this model.

5.2. Outline of the Baseline Simulation

[22] Using the model, we discuss the relationships between the ice fraction (A_i), ice thickness (h), and tempera-

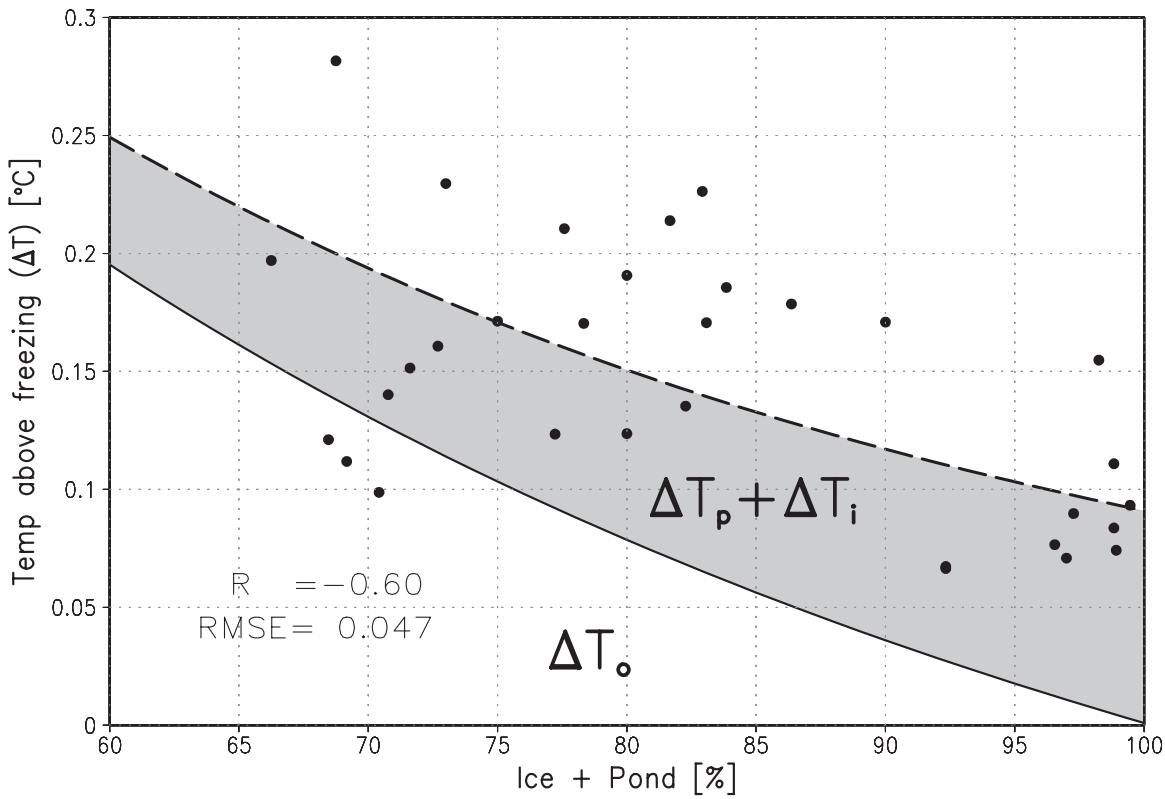

Figure 6. Scatterplots of the ice concentration (A_p + A_i) versus temperature above the freezing point (ΔT). Daily mean ice concentration was derived from the on-board ice-watch, and ΔT data were calculated from XCTD observations. The dashed line is a regression based on the observations. *R* and *RMSE* indicate the correlation coefficient and root mean square error, respectively. The solid line is the same line subtracted from the Δ *T*-bias (=0.09 K) from the regression line weighted by ice concentration. The shaded area denotes the $\Delta\ T_p + \Delta\ T_i$.

ture above the freezing point (ΔT). Here, all parameters are set to values suitable for the observational region. We set *H* at 15 m on the basis of the temperature and salinity profiles from Figure 4. The net heat input at the surface F_n is set to a constant value.

[23] Initial ΔT and h_0 equaled 0.0 K (i.e., the freezing point) and 1.5 m, respectively. However, several calculations were done using different initial ice concentration (A_{i0}) and heat input (F_n) by changing from 30% to 99%, and from 10 W m^{-2} to 150 W m^{-2}, respectively. Hereafter, we call this experiment set RUN_O, in which we only included the heat input from open water. To compare the modeled results with our observation, the output from RUN_O using F_n = 110 W m^{-2} (baseline case) is suitable because the averaged incoming SW radiation during August is nearly 110 W m^{-2} around the region [*Persson et al.*, 2002; *Inoue et al.*, 2005b; Figure 3].

5.3. Results Without the Effects of Heat Transmission Through Ponds and Ice

[24] CT-relationships converge asymptotically to a single curve with a timescale of ~10 days regardless of initial conditions of A_i and ΔT [*Ohshima et al.*, 1998; *Ohshima and Nihashi*, 2005]. Closed circles in Figure 8 show the CT-plot after 15 days of the integration of RUN_O. In this calculation, ΔT is zero under the completely ice-covered situation due to the lack of heat input through open water. In other words, the modeled ΔT-gain is comparable to the analyzed ΔT_o. Both lines are closely matched, suggesting that the model can appropriately describe the heat transfer through open water.

[25] To examine the sensitivity of F_n, the results with 110 ± 10 W m^{-2} are plotted in Figure 9 (note the lower abscissa in reverse). The differences of ΔT from the baseline case is ±0.01 K under a 30% fraction of open water (observed A_o ranges from 0 to 40%). Therefore the sensitivity of F_n seems to be small in the highly ice-covered region.

[26] Since we already know the relationship between A_p and ΔT_p, and between A_i and ΔT_i (Figure 8), we can indirectly estimate how much heat input is required to obtain the ΔT from ponded and ice-covered areas by using the results of RUN_O (Figure 9). The heat input corresponding to the relationship between A_p (from 20 to 25% in the observation) and ΔT-gain ranges between 40 and 80 W m^{-2}, while that for A_i ranges around 10 W m^{-2}. These values for A_p and A_i are considered to be the transmitted heat through ponds and ice that should be basically much smaller than F_n(=110 W m^{-2}), because most of the incoming SW radiation is reflected at the pond and ice surfaces.

[27] Here, we calculated the transmittance of ponds (τ_p) and ice (τ_i) using these values. To gain the same amount of ΔT only through ponds and ice, $\tau_p F_n$(=60 ± 20 W m^{-2}) and $\tau_i F_n$(=10 W m^{-2}) are the respective heat inputs into the ocean (Figure 9). Thus the heat transmittances of ponds

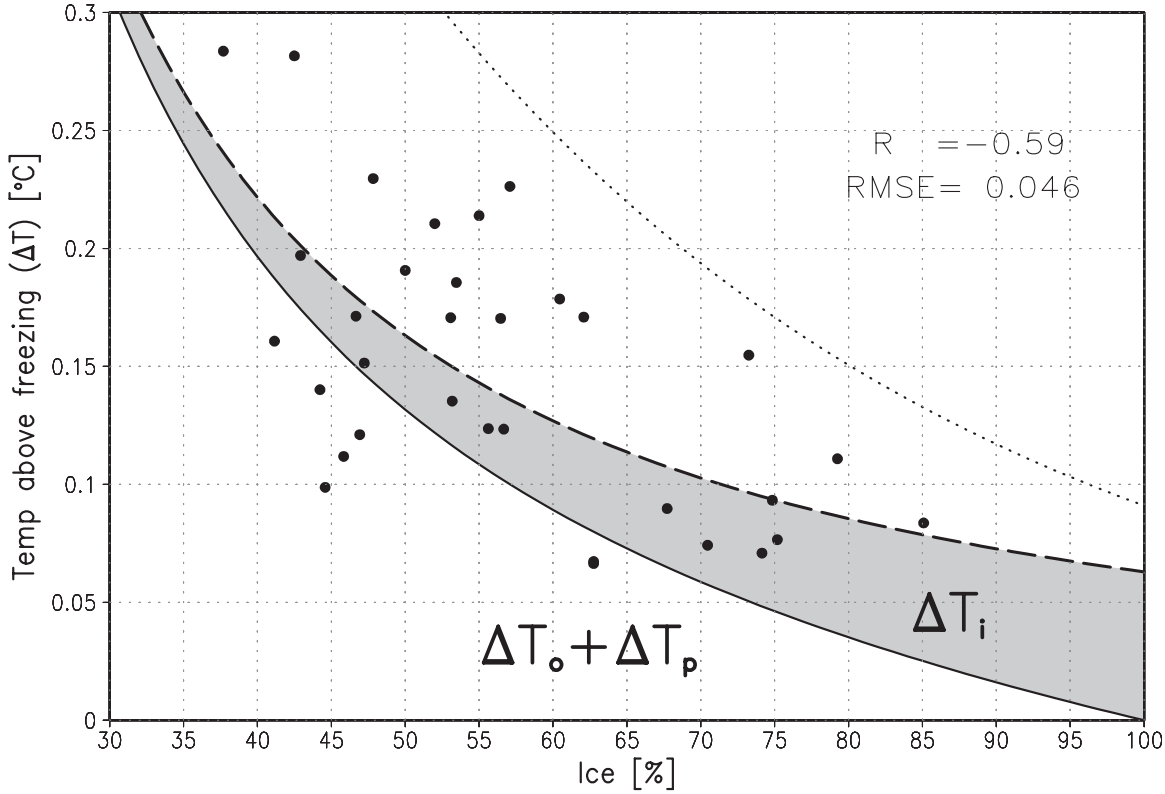

Figure 7. As in Figure 6, but showing A_i versus ΔT. The shaded area denotes ΔT_i. The dotted line is the same as the dashed line in Figure 6, but the range of the lower abscissa is expanded.

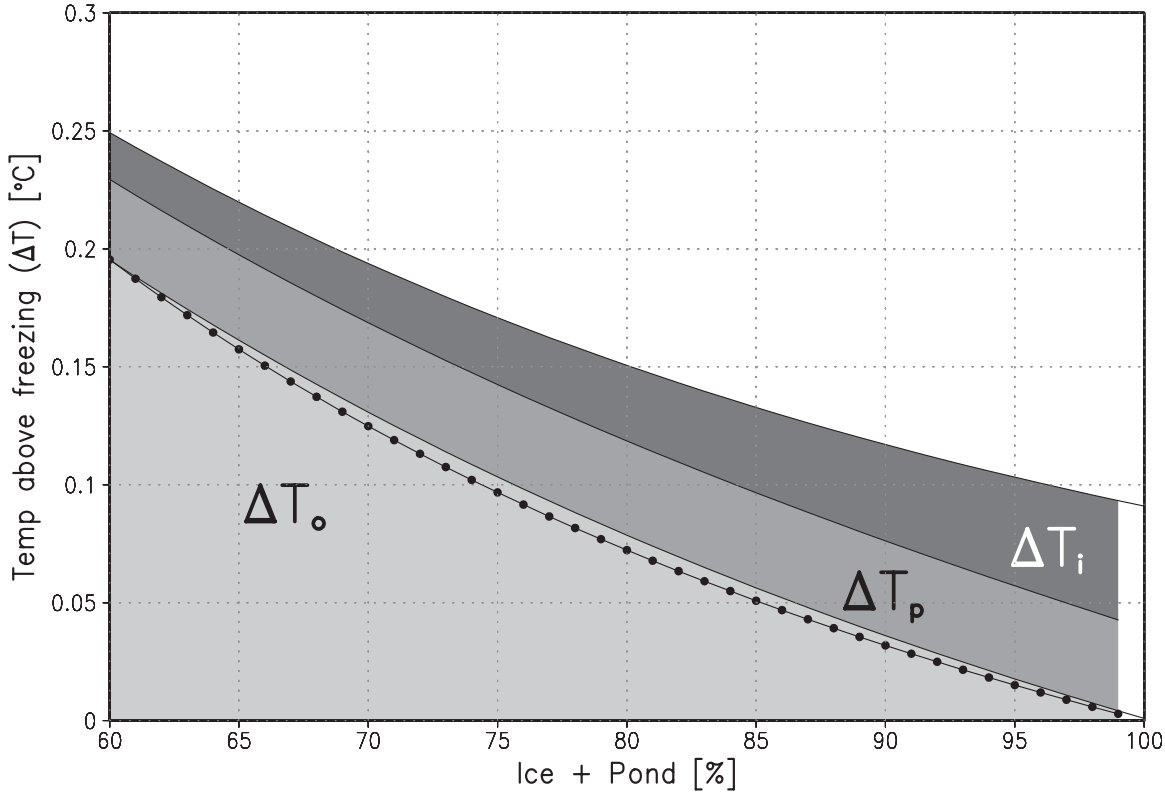

Figure 8. ΔT-gain from open water, melt ponds, and ice as a function of $A_i + A_p$. Closed circles are model results by RUN_O using F_n = 110 W m^{-2} after 15 days of the time integration.

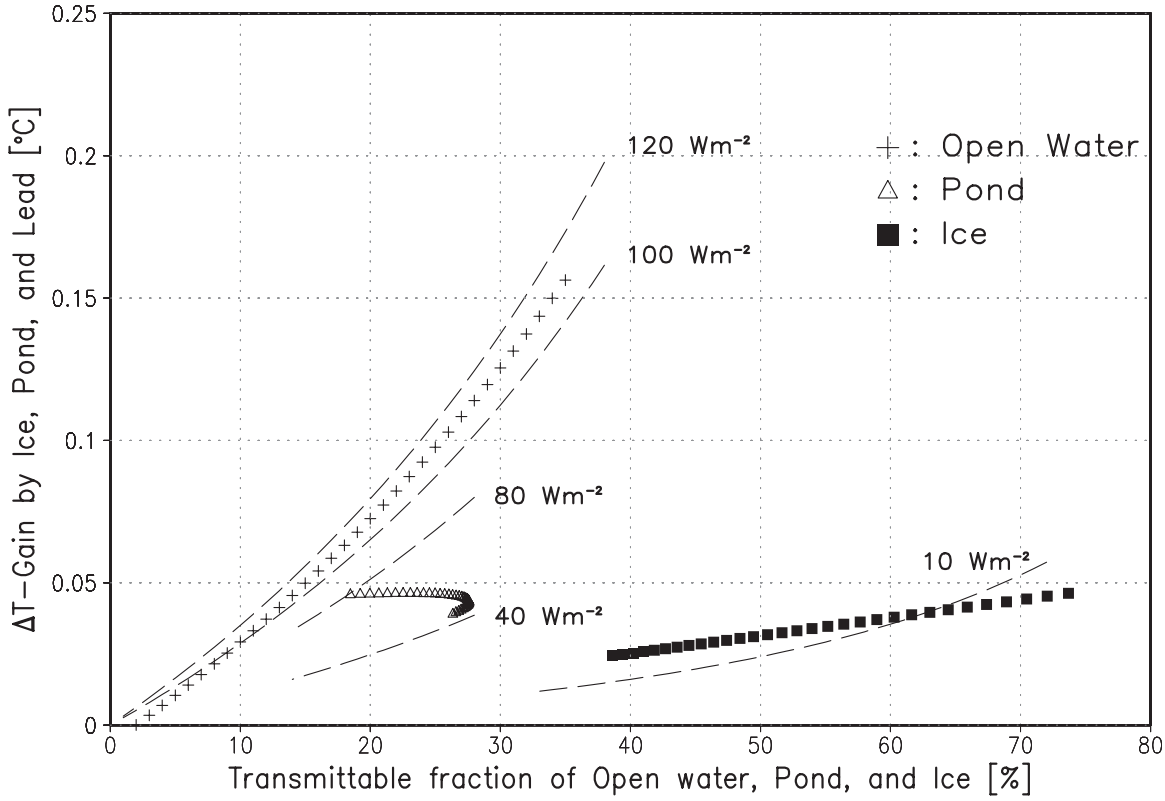

Figure 9. ΔT-gain induced by open water, melt ponds, and ice. These relationships are obtained by the regression lines in Figure 8. The lower abscissa shows each fraction for A_o, A_p, and A_i, respectively. Dashed lines denote model results (RUN_O) induced by different heat inputs F_n.

(τ_p= 60 ± 20/110 = 0.55 ± 0.18) and ice (τ_i = 10/110 = 0.09) are obtained. These two values suggest that sea-ice transmits little SW radiation, while melt ponds have an intermediate characteristic between open water and sea-ice. Therefore even if the A_p is smaller than A_i as we observed, the pond contribution to the ΔT-gain is almost the same (Figure 8).

5.4. Effects of Heat Transmission Through Ponds and Ice on Melting

[28] Using τ_p and τ_i, the effect of melt ponds and ice on the melting processes can be examined by including the additional terms related to these parameters into equation (1) as,

$$c_w \rho_w H \frac{dT}{dt} = F_n\left(\tau_o A_o + \tau_p A_p + \tau_i A_i\right) + L_f \rho_i \left(\left(A_p + A_i\right) \frac{dh}{dt} + h \frac{d\left(A_p + A_i\right)}{dt} \right), \quad (4)$$

where the transmittance of open water ($\tau_o = 1 - \alpha_o = 0.94$), ponds ($\tau_p$ = 0.55), and ice (τ_i = 0.09) is a fixed value, respectively. In this model framework, A_p is also given as a function of A_i obtained from Figure 7 (A_p ranges from 20% to 25% at any A_i). In addition, the depth of melt ponds is not treated in this model. Other initial conditions are the same as in RUN_O. Hereafter, this experiment set is referred to as RUN_{ALL} and includes the heat input from all surface categories.

[29] Figure 10 shows the convergence curves of RUN_{ALL} (solid line) and RUN_O (dashed line) after 15 days of the integration, respectively. Clearly, RUN_{ALL} has a bias of about 0.06 K under highly ponded and ice-covered situations (e.g., $A_p + A_i$ = 99%), which almost agrees with the observed CT-relationship (dots in Figure 10). Without the heat transmission from ponds and ice (RUN_O), ΔT would not be so large (dashed line).

[30] Because this higher ΔT in RUN_{ALL} is a consequence of heat balance in the ice-upper ocean system, the ice concentration and ice thickness should also vary differently between RUN_O and RUN_{ALL}. Figure 11 shows the changes over time of ice thickness and ice concentration ($A_p + A_i$) when the initial open water fraction (A_{o0}) is set to 3% for RUN_{ALL} and RUN_O. The difference in the decrease in ice thickness between the two runs is less than 0.1 m after 15 days of the integration. Interestingly, the decrease in ice concentration is linked to the decrease in ice thickness, particularly for RUN_{ALL}. A possible explanation for this may be that because the total extent of the lateral faces of relatively thin ice is small, less heat is used in lateral melting, thus enhancing the increase in ΔT. As ΔT becomes greater, $A_p + A_i$ and h decrease further. The lower $A_p + A_i$ and thinner h further enhance the increase in ΔT, promoting the open water-albedo feedback [*Ackley et al.*, 2001].

[31] In the case of RUN_O, on the other hand, ice thickness and concentration hardly change due to the lack of heat input from ponds and ice as well as from open water. Therefore the effect of transmitted heat through ponds and

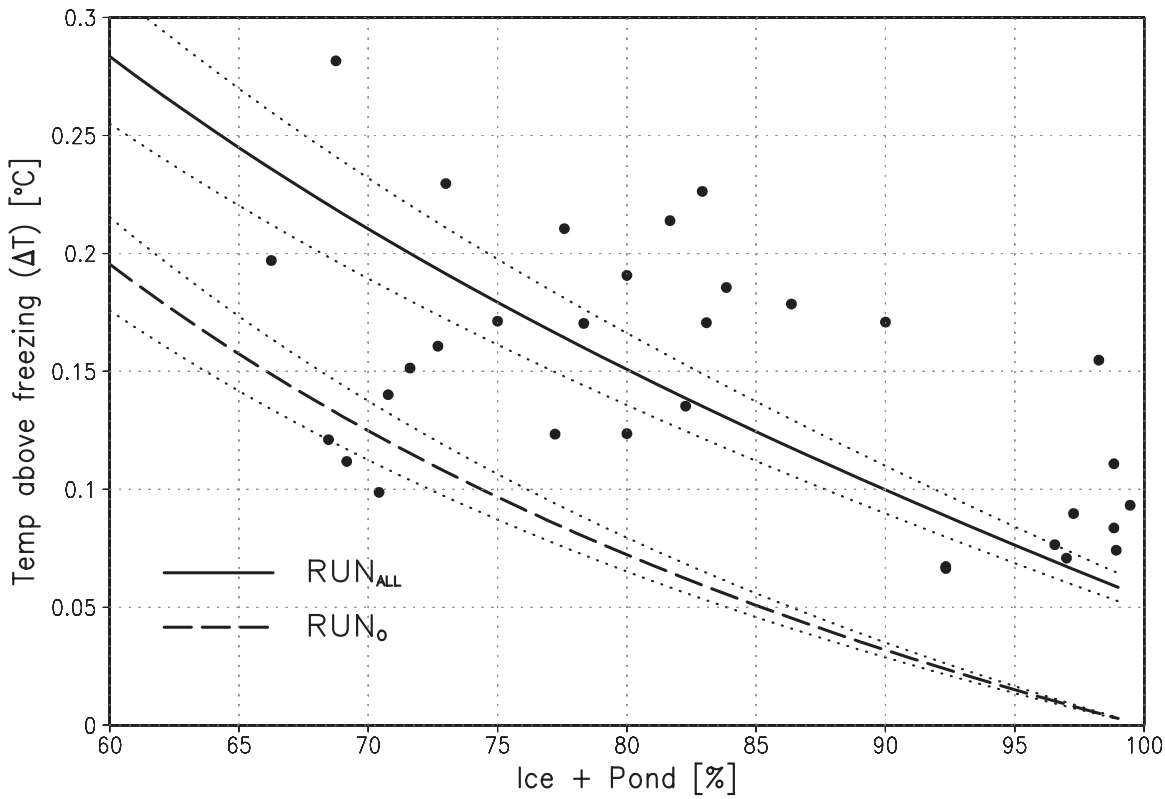

Figure 10. As in Figure 6, but showing model results with heat transmittance by melt ponds and ice (solid line, RUN_{ALL}), and without their effects (dashed line, RUN_O). Dots show the observational results; doted lines show the results calculated using F_n = 110 ± 10 W m^{-2}.

ice significantly affects the open water-albedo feedback process, particularly in highly ice-covered regions.

5.5. Effects of Transmitted Heat Through Ponds and Ice on the Open Water-Albedo Feedback

[32] How is the open water-albedo feedback amplified by the transmitted heat through ponds and ice? To assess the strength of this feedback, we additionally compared perturbed simulations that included heat input through ponds and ice areas with a corresponding perturbed simulation that did not include these effects. The strength of the feedback may be quantified by defining the feedback gain ratio R_f [*Curry et al.*, 2001]:

$$R_f(h) = \frac{\Delta h_{on}}{\Delta h_{off}}, \tag{5}$$

where h is the ice thickness as the climate parameter, Δ denotes the change in h associated with a specified forcing, and the subscripts *on* and *off* indicate that the heat input through ponds and ice areas are turned on and off, respectively. A positive value of $R_f(h)$ greater than 1.0 indicates a positive feedback mechanism; $R_f(h)$ varies with the sign and the magnitude of the forcing. Four different model simulations are required to obtain $R_f(h)$:

[33] (1) a baseline simulation using equation (1), representing the current unperturbed conditions without heat transmission of ponds and ice;

[34] (2) a simulation using equation (1) in which the climate is subject to an external perturbation and heat transmission of ponds and ice are turned off;

[35] (3) a simulation using equation (4), representing the current unperturbed conditions with heat transmission of ponds and ice;

[36] (4) a simulation using equation (4) in which the climate is subject to an external perturbation and heat transmission of ponds and ice is operative.

[37] A warming perturbation is given as 4 W m^{-2}, which is comparable to the doubled CO_2 forcing [*Ramanathan et al.*, 1989]. The feedback gain ratio is then evaluated from

$$R_f(h) = \frac{h_4 - h_3}{h_2 - h_1}, \tag{6}$$

where the numerical subscripts refer to the above enumerated model simulations.

[38] Figure 12 shows $R_f(h)$ as a function of initial ice concentration ($A_p + A_i$) after 15 days of the integration. In the case of relatively high initial ice concentration (e.g., ≥95%), the large $R_f(h)$ suggests that bottom melting was significantly amplified (i.e., $\Delta h_{on} \gg \Delta h_{off}$), because the heat input through ponds and ice overwhelms that from open water. In contrast, in the case of lower ice concentration, the feedback by this effect is small because heat input from open water is the main source of energy, although positive feedback still operates ($R_f(h) \geq 1$). The result of $R_f(ice)$ is also the same as $R_f(h)$ (data not shown), suggesting that the heat transmitted through ponds and ice areas

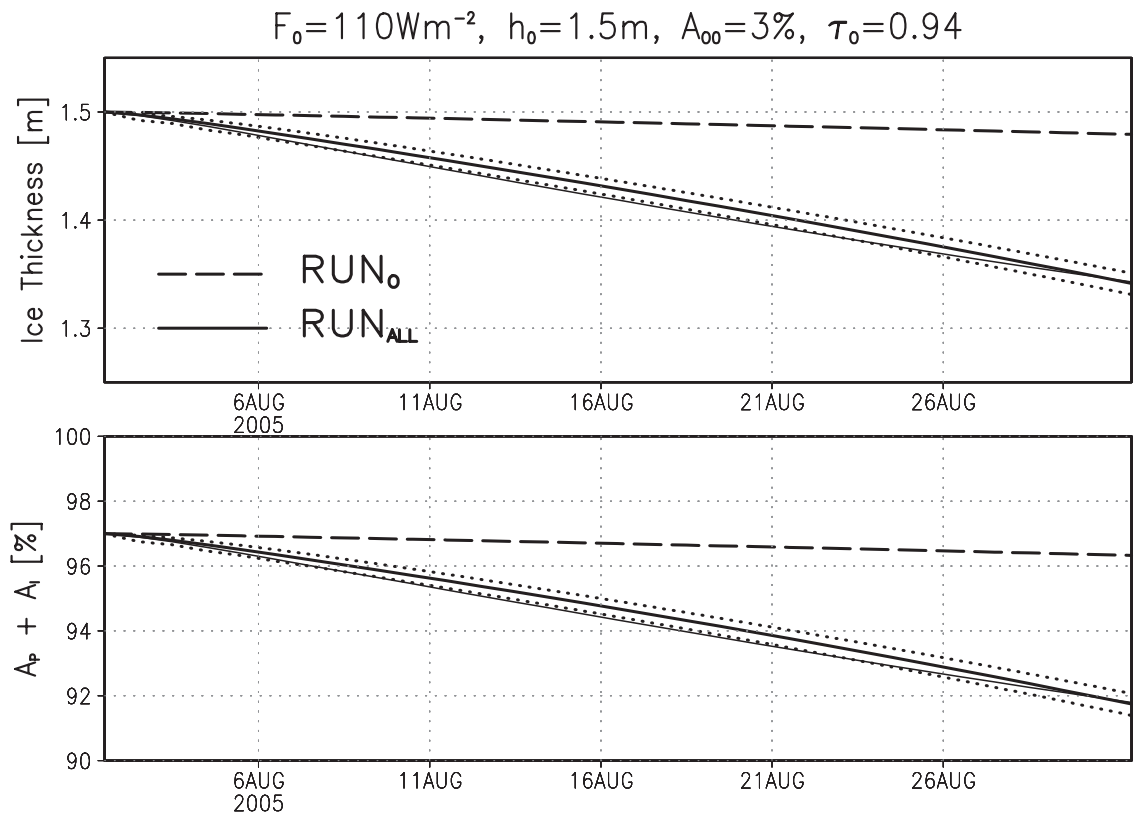

Figure 11. Evolution of ice thickness (top) over time and ice concentration ($A_p + A_i$: bottom). Solid and dashed lines denote the cases where the effects of heat transmittance of melt ponds and ice are turned on (RUN_{ALL}) and off (RUN_O), respectively. The same runs as RUN_{ALL} but H is varied 15 ± 10 m (dotted lines) and a realistic F_n is given (thin solid line).

significantly affects the open water-albedo feedback in the highly ice-covered region. Of course, this feedback would be largely affected by the ice thickness distribution. *Ebert et al.* [1995] showed that the net transmission of solar radiation into the ocean is roughly 30% greater for a distribution of ice thicknesses categorized differently than for a single ice slab (e.g., this study) under the same mean ice thickness. Thus the feedback might be stronger in fact than modeled one.

6. Summary and Discussion

[39] The XCTD observations and ice monitoring during the trans-Arctic cruise in the summer of 2005 revealed that the temperature above freezing (ΔT) in the surface mixed layer is a function of the ice concentration (CT-relation: Figure 6). This is a consequence of heat balance in the ice-upper ocean system, which consists of heat input, ice melting, and heat storage in the mixed layer. In the Antarctic Ocean, this relationship is clear when 20–30-km running mean data were used [*Ohshima et al.*, 1998]. This suggests that the local heat balance in the ice-upper ocean system approximately holds over that spatial scale, while at smaller spatial scales, ice advective effects predominate. In our case, the spatial running mean is not effective because the XCTD stations are sparsely located; instead, daily running mean sea-ice data were used. If we assume the free drift of ice as 2% of wind speed (typically ~5 m s^{-1}), the ice travels ~10 km per day. Considering the ship's speed (around 100 km per day), the spatial scale to interact with the upper ocean by ice drifting corresponds to 10 days or more.

[40] In the analyzed CT-relationship, there is a positive bias of ΔT in the highly ice-covered area, suggesting that melt ponds and sea ice allow significant heat input to the ocean by transmitting SW radiation. By partitioning the gain of ΔT into the components of open water, ponds, and ice, we found that the role of ponds and ice areas is significantly large in the highly ice-covered area (Figure 8), which enhances bottom melting without heat input from open water. From these results, the respective transmittance of ponds (0.55) and ice (0.09) was evaluated. These transmittances should vary as surface conditions change depending on the melting stages (e.g., before melt onset, melting period, and freezeup).

[41] Considering that our analysis was based on observations made during August, the transmittances for ponds (0.55) and bare ice (0.09) have reached a maximum, which is consistent with results of *Perovich* [2005]. In fact, at the beginning of the cruise, we saw very mature ponds with a low albedo, and thin ice at the bottom of the pond (Figure 2). Although the transmittances might vary from place to place depending on the ice thickness and pond depth, our results represent the case of relatively thin ice with a minimum ice thickness of ~1.5 m during late summer (Figure 5d).

[42] Using a simple ocean-ice-coupled model, we examined the effects of transmitted heat through ponds and ice on the open water-albedo feedback mechanism. A comparison

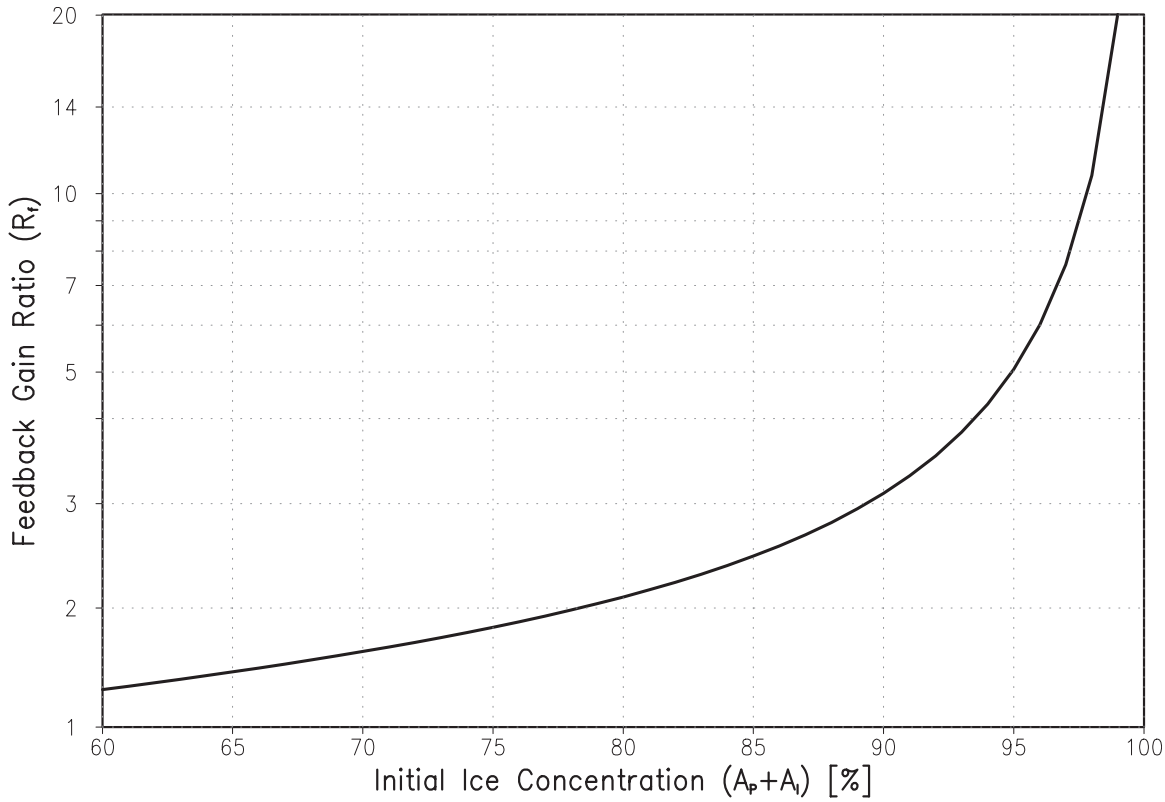

Figure 12. Feedback gain ratio for the effect of transmitted heat through ponds and ice on the bottom melting as a function of the initial ice concentration (A_p + A_i). Results are based on 15 days of the integration with perturbed heat flux.

between the modeled results by turning the effects on and off showed that the decrease in ice thickness is enhanced by these effects and amplifies the open water-albedo feedback. Because our model is very simplified, time evolutions of the ponded fraction (A_p), thickness of the mixed layer (H), seasonal changes in heat input (F_n), and horizontal oceanic heat advection may be sources of errors. In general, the ponds begin forming in early June shortly after snowmelt, and a discrete jump in the pond fraction from 5% to 20% occurs during mid-June. Then there is a steady and gradual increase in the pond fraction exceeding 20% [*Perovich*, 2005]. Therefore our modeled results using the fixed value of A_p is probably applicable under a short time integration (e.g., less than 1 month), particularly by focusing on the ice-upper ocean system during late summer, although the sensitivity of FYI ablation depends on pond fraction and the associated spatial variability in surface albedo [*Hanesiak et al.*, 2001].

[43] As for the thickness of the mixed layer H, we have checked its sensitivity by perturbing $H = 15 \pm 10$ m (dotted lines in Figure 11). Ice melts relatively quickly when H is relatively shallow because ΔT readily increases, and vice versa in the case where H is deeper. However, the differences in ice thickness and ice concentration are very small between the runs. With regard to the seasonal change of F_n, we conducted an additional sensitivity run using one-third of the time-dependent SW radiation at the top of atmosphere, which has been verified by *Inoue et al.* [2005b]. Although F_n decreases from 140 to 80 W m^{-2} during August as in Figure 3, changes in ice thickness and ice concentration are very small compared to RUN_{ALL} (thin solid line in Figure 11). We also did not consider the contribution of net longwave radiation and turbulent heat flux to F_n because they are near zero during August [*Persson et al.*, 2002]. Therefore the fixed value of F_n given as SW radiation is presumably appropriate unless the time integration is too long (~2 weeks). Although the role of horizontal oceanic heat advection is not treated in our model, its effect is the secondary one because the difference between the observed ΔT(=0.09 K) and modeled ΔT(=0.06 K) in the completely ice-covered area is smaller than the effect of heat transmission.

[44] In conclusion, in modeling Arctic sea-ice melting, the inclusion of heat input through melt ponds and ice areas is of major importance in highly ice-covered regions, and even a simplified model that neglects other effects can describe the fundamental features of ice melt during a short timescale. CT-relationship in the Arctic Ocean introduced in this study could be a good indicator to verify the heat balance in the upper ocean system simulated by climate models used in the Intergovernmental Panel on Climate Change (IPCC), for example.

[45] **Acknowledgments.** We sincerely thank all participants on-board USCGC *Healy*. We are deeply indebted to Kazutaka Tateyama, Hirokatsu Uno, Bruce Elder, Tom Grenfell, and Jeremy Harbeck for their help with the ice-watch. Suggestions and comments from anonymous reviewers and associate editor were very helpful. Support for this study was provided by the Japan Agency for Marine-Earth Science and Technology (JAMSTEC) and the National Science Foundation (NSF) under Grant No. ARC-0454900.

References

Ackley, S. F., C. A. Geiger, J. C. King, E. C. Hunke, and J. Comiso (2001), The Ronne polynya of 1997–1998: Observations of air-ice-ocean interaction, *Ann. Glaciol.*, *33*, 425–429.

Cavalieri, D., P. Gloerson, and W. J. Cambbell (1984), Determination of sea ice parameters with the Nimbus 7 SMMR, *J. Geophys. Res.*, *89*(D4), 5355–5369.

Cavalieri, D., P. Gloerson, and J. Zwally (1990), *DMSP SSM/I Daily Polar Gridded Sea Ice Concentrations, June to September 2001* [digital media], edited by J. Maslanik and J. Stroeve, National Snow and Ice Data Center, Boulder, Colo.

Comiso, J. (1990), *DMSP SSM/I Daily Polar Gridded Sea Ice Concentrations*, June to September 2001 [digital media], edited by J. Maslanik and J. Stroeve, National Snow and Ice Data Center, Boulder, Colo.

Curry, J. A., J. L. Schramm, and E. E. Ebert (1995), Sea ice-albedo climate feedback mechanism, *J. Clim.*, *8*, 240–247.

Curry, J. A., J. L. Schramm, D. K. Perovich, and J. O. Pint (2001), Applications of SHEBA/FIRE data to evaluation of snow/ice albedo parameterizations, *J. Geophys. Res.*, *106*(D14), 15,345–15,356.

Darby, D. A., M. Jakobsson, and L. Polyak (2005), Icebreaker expedition collects key Arctic seafloor and ice data, *Eos Trans. AGU*, *86*(52), 549–552.

Ebert, E. E., J. L. Schramm, and J. A. Curry (1995), Disposition of solar radiation in sea ice and the upper ocean, *J. Geophys. Res.*, *100*(C8), 15,965–15,975.

Eicken, H., M. Lensu, M. Leppäranta, W. B. Tucker III, A. J. Gow, and O. Salmela (1995), Thickness, structure, and properties of level summer multiyear ice in the Eurasian sector of the Arctic Ocean, *J. Geophys. Res.*, *100*(C11), 22,697–22,710.

Fetterer, F., and N. Untersteiner (1998), Observations of melt ponds on Artic sea ice, *J. Geophys. Res.*, *103*(C11), 24,821–24,835.

Grenfell, T. C., and G. A. Maykut (1977), The optical properties of ice and snow in the Arctic Basin, *J. Glaciol.*, *18*(C3), 445–463.

Grenfell, T. C., and D. K. Perovich (1984), Spectral albedos of sea ice and incident solar irradiance in the southern Beaufort Sea, *J. Geophys. Res.*, *89*(C3), 3573–3580.

Grenfell, T. C., and D. K. Perovich (2004), Seasonal and spatial evolution of albedo in a snow-ice-land-ocean environment, *J. Geophys. Res.*, *109*, C01001, doi:10.1029/2003JC001866.

Hanesiak, J. M., J. J. Yackel, and D. G. Barber (2001), Effect of melt ponds on first-year sea ice ablation – Integration of RADARSAT-1 and thermodynamic modelling, *Can. J. Remote Sens.*, *27*(5), 433–442.

Hibler, W. D., III (1979), A dynamic thermodynamic sea-ice model, *J. Phys. Oceanogr.*, *9*, 815–846.

Inoue, J., and T. Kikuchi (2006), Effect of summertime wind conditions on lateral and bottom melting in the central Arctic, *Ann. Glaciol.*, *44*, 37–41.

Inoue, J., B. Kosovic, and J. A. Curry (2005a), Evolution of a storm-driven cloudy boundary layer in the Arctic, *Boundary Layer Meteorol.*, *117*(2), 213–230.

Inoue, J., T. Kikuchi, D. K. Perovich, and J. H. Morison (2005b), A drop in mid-summer shortwave radiation induced by changes in the ice-surface condition in the central Arctic, *Geophys. Res. Lett.*, *32*(13), L13603, doi:10.1029/2005GL023170.

Inoue, J., J. A. Curry, and J. A. Maslanik (2008), Application of Aerosondes to melt-pond observation over Arctic sea ice, *J. Atmos. Oceanic Technol.*, *25*(2), 327–334.

Intrieri, J. M., M. D. Shupe, T. Uttal, and B. J. McCarty (2002), An annual cycle of Arctic cloud characteristics observed by radar and lidar at SHEBA, *J. Geophys. Res.*, *107*(C10), 8029, doi:10.1029/2000JC000423.

Liu, J., Z. Zhang, J. Inoue, and R. M. Horton (2006), Evaluation of snow/ice albedo parameterizations and their impacts on sea ice simulations, *Int. J. Climatol.*, *27*(1), 81–91.

Maykut, G. A., and G. M. McPhee (1995), Solar heating of the Arctic mixed layer, *J. Geophys. Res.*, *100*(C12), 24,691–24,703.

Maykut, G. A., and D. K. Perovich (1987), The role of shortwave radiation in the summer decay of a sea ice cover, *J. Geophys. Res.*, *92*(C7), 7032–7044.

McPhee, M. G., T. Kikuchi, J. H. Morison, and T. P. Stanton (2003), Ocean-to-ice heat flux at the North Pole Environmental Observatory, *Geophys. Res. Lett.*, *30*(24), 2274, doi:10.1029/2003GL018580.

Nihashi, S., K. I. Ohshima, M. O. Jeffries, and T. Kawamura (2005), Sea ice melting processes inferred from ice-upper ocean relationship in the Ross Sea, Antarctica, *J. Geophys. Res.*, *110*, C02002, doi:10.1029/2003JC002235.

Ohshima, K. I., and S. Nihashi (2005), A simplified ice-ocean coupled model for the Antarctic ice melt season, *J. Phys. Oceanogr.*, *35*, 188–201.

Ohshima, K. I., K. Yoshida, H. Shimoda, M. Wakatsuchi, T. Endoh, and M. Fukuchi (1998), Relationship between the upper ocean and sea ice during the Antarctic melting season, *J. Geophys. Res.*, *103*(C4), 7601–7615.

Perovich, D. K. (2005), On the aggregate-scale partitioning of solar radiation in Arctic sea ice during the Surface Heat Budget of the Arctic Ocean (SHEBA) field experiment, *J. Geophys. Res.*, *110*, C03002, doi:10.1029/2004JC002512.

Persson, P. O. G., C. W. Fairall, E. L. Andreas, P. S. Guest, and D. K. Perovich (2002), Measurements near the atmospheric surface flux group tower at SHEBA: Near-surface conditions and surface energy budget, *J. Geophys. Res.*, *107*(C10), 8045, doi:10.1029/2000JC000705.

Ramanathan, V., R. D. Cess, F. F. Harrison, P. Minnis, B. R. Barkstrom, E. Ahmad, and D. Hartman (1989), Cloud-radiative forcing and climate: Results from the Earth Radiation Budget Experiment, *Science*, *243*, 57–63.

Richter-Menge, J. A., D. K. Perovich, and W. S. Pegau (2001), Summer ice dynamics during SHEBA and its effect on the ocean heat content, *Ann. Glaciol.*, *33*, 201–206.

Shimada, K., E. C. Carmack, K. Hatakeyama, and T. Takizawa (2001), Varieties of shallow temperature maximum waters in the western Canadian Basin of the Arctic Ocean, *Geophys. Res. Lett.*, *28*(18), 3441–3444.

Steele, M. (1992), Sea ice melting and floe geometry in a simple ice-ocean model, *J. Geophys. Res.*, *97*(C11), 17,729–17,738.

Worby, A. P., and I. Allison (1999), A technique for making ship-based observation of Antarctic sea ice thickness and characteristics: I. Observational techniques and results, *Res. Rep.*, vol. 14, pp. 1–23, Antarct. Coop. Res. Cent., Hobart, Tasmania, Australia.

J. Inoue and T. Kikuchi, Institute of Observational Research for Global Change, Japan Agency for Marine-Earth Science and Technology, 2–15 Natsushima-cho, Yokosuka, Kanagawa 237-0061, Japan. (jun.inoue@jamstec.go.jp)

D. K. Perovich, Engineer Research and Development Center, Cold Regions Research and Engineering Laboratory, 72 Lyme Road, Hanover, NH 03755, USA.